Mechanisms of holographic recording in rubidium vapor close to resonance

N. Korneev[1,*] and O. Benavides[2]

[1]*Instituto Nacional de Astrofísica, Óptica y Electrónica, A.P. 51 y 216, CP 72000, Puebla, Mexico*
[2]*Universidad Autónoma del Carmen, Cd. del Carmen, Campeche, Mexico*
**Corresponding author: korneev@inaoep.mx*

Received June 19, 2008; revised September 1, 2008; accepted September 9, 2008; posted September 15, 2008 (Doc. ID 97697); published October 27, 2008

We investigate the nonlinear refraction and absorption related to holographic writing in rubidium vapor at resonance with ^{87}Rb D2 transition. The numerical model based on time-dependent density matrix formalism is used. The theory adequately describes nonlinear optical rotation and absorption at light intensities in the 0.1–30 mW/cm^2 range. The basic configurations for obtaining amplitude and phase gratings for nearly equal frequencies of writing beams are investigated experimentally, and the writing time is estimated. © 2008 Optical Society of America

OCIS codes: 090.7330, 190.4223.

1. INTRODUCTION

Dynamic holographic media, photorefractive materials in particular, have been proposed for a number of applications, including real-time holographic interferometry, phase conjugation, image processing, filters, memory, etc. [1]. The rubidium vapor as holographic material has some exceptional properties. The gratings can be written in it with tunable semiconductor lasers at resonance with D1 or D2 lines (795 or 780 nm). The characteristic intensity for writing $I \geq 1$ mW/cm^2 is determined by line saturation. The writing time can be estimated with the upper level lifetime (25 ns), or by the time in which the atom crosses the interference fringe (≈ 0.5 μs for 100 μm fringe width). We demonstrate here that amplitude gratings with $\approx 1\%$ diffraction efficiency can be produced at $I \approx 10$ mW/cm^2 with writing time of less than 10^{-7} s. Thus, the sensitivity parameter of rubidium S^{-1}, equal to the energy per area necessary for 1% effective hologram [2], is estimated as $S^{-1} \approx 10^{-9}$ J/cm^2. This is four orders of magnitude better than $S^{-1} \approx 10^{-5}$ J/cm^2 reported for fast photorefractive semiconductors InP and GaAs [2]. For higher intensities, efficient phase gratings can be written as well. Rubidium cells are not expensive and have excellent optical quality and a big cross section. On the other hand, exact wavelength tuning, sample heating, and magnetic field control are needed.

Though the resonant interaction of light with rubidium is a field of active study in quantum optics and nonlinear spectroscopy, relatively little attention has been paid to holography in this material. Phase conjugation with four-wave mixing was reported in [3,4], and the geometry using nonlinear Faraday rotation was reported in [5]. The related topics of self-focusing and nonlinear waveguiding were studied in [6–10]. The two-level atom model was used to describe experiments for a laser wavelength detuned at 0.5–1 GHz from the Doppler-broadened to the 0.5 GHz absorption line [9,10]. Such an arrangement gives moderate nonlinear coefficients around 10^{-7} cm^2/W [9] for 78°C and up to 10^{-5} cm^2/W for higher temperatures [6,7]. Experiments demonstrate that saturation and quantum coherence effects can strongly enhance the nonlinear coefficients when the laser is directly tuned to resonance [5,8,10]. In particular, the nonlinear Faraday rotation at 32°C and 1 mW/cm^2 is ≈ 0.5 rad/m [5]. This gives, taking into account the 60 times difference in vapor density between 32°C and 78°C [11,12], that the characteristic nonlinear coeffficient at 78°C is in the 10^{-3} cm^2/W range. However, these higher values are usually accompanied by stronger absorption.

We discuss here two principal mechanisms. The first is based on absorption grating writing. In [5] we experimentally investigated another grating formation mechanism based on Faraday rotation. It is promisimg for applications because it results in phase holograms with higher diffraction efficiency. Here we develop the theory for both cases. The experimental part of this paper in some points is closely related to [5], and we will refer to it where appropriate.

The microscopic description of hologram formation starting from basic principles can be done for rubidium, but adequate theory is complex because of the big number of sublevels involved (Fig. 1). At resonance, complicated polarization behavior emerges, and the geomagnetic field can radically change the observed polarization properties and diffraction efficiency. The strong dependence on the time of transit is also observed. In particular, the measured light absorption for $F_g = 1$ in the D2 ^{87}Rb transition is affected by the beam diameter. There is little hope that a tractable analytical solution can account for all of these factors. The theory for the resonant case, as far as we know, was not developed in detail.

We study a realistic computer model based on density matrix formalism. The number of participating sublevels for our experimental conditions is up to 15, which means

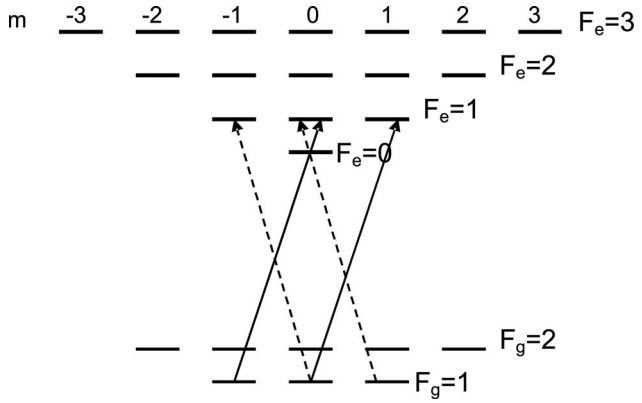

Fig. 1. Sublevel structure for ^{87}Rb D2 line. Numbers −3…3 are momentum projections on quantization z axis m_F. Energy differences between levels are not to scale. As an example, the transitions induced by right (solid arrows) and left circular polarizations (dashed arrows) between $F_g=1$ and $F_e=1$ levels are shown.

solving up to 225 coupled linear differential equations for matrix elements. Additionally, integration with respect to detunings is needed to account for Doppler broadening. The temporal evolution of the matrix is calculated, which permits us to include important effects of transit. The task is implemented in an acceptable time (minutes to hours) with a special code written in C. The full solution gives a highly detailed description, including sublevel population dynamics, and relative importance of different F levels for the particular process. Though the model is quite involved, good agreement with the experiment makes it a useful guide. In some cases, simplified approximations can be derived.

The outline of this article follows. First, we describe the computer model and results for intensity-dependent absorption and optical activity for uniform illumination. Next, experimental measurements of absorption and optical rotation are reported and compared with the theory. The experiments with absorption and phase gratings are described. The last part presents discussion and conclusions.

2. COMPUTER MODEL, DESCRIPTION

For reasons of computation complexity we investigate only one of two naturally present isotopes, ^{87}Rb, which has a smaller number of sublevels. This isotope produces more efficient gratings for the conditions of our earlier experimental work [5]. The structure of transitions for the isotope is depicted in Fig. 1. The ground level is split into two hyperfine components with $F_g=1$ and $F_g=2$ representing full momentum, separated by 6.83 GHz. These levels in the presence of the magnetic field are further subdivided into 3 and 5 Zeeman components, respectively, with $m_F=-F,\ldots F$. The excited manifold consists of four hyperfine levels with $F_e=0,1,2,3$. These levels also have Zeeman sublevels according to their F numbers. The hyperfine splittings between the upper levels are 72 MHz, 157 MHz, and 267 MHz. As the characteristic Doppler broadening is 0.5 GHz, the transitions within the upper manifold are not resolved, and the experimentally observed absorption spectrum has two lines with ≈7 GHz separation. A detailed review of spectroscopic data for ^{87}Rb can be found in the online reference [11].

To simplify the problem, we normally assume that the light of a given frequency interacts only with the closest F level of the upper manifold of an atom with a definite Doppler shift. This assumption breaks for the $F_g=1$ line at the high end of the experimentally investigated intensities 5–30 mW/cm^2, where the light of a given frequency can interact simultaneously with two close levels, $F_e=0$ and $F_e=1$. The situation manifests itself in one upper-level model when the width of characteristic spectral features become comparable to the $F_e=0$ and $F_e=1$ frequency difference of 72.2 MHz. For even higher intensities, all three upper levels of permitted transition are necessary. Though our software can handle the complete task, the solution substantially slows down the process. Thus we consider independent interaction with all F_e levels, with the exception of the transition $F_g=1$, $F_e=0,1$, which is treated separately. For the ground manifold, both $F_g=1$ and $F_g=2$ sublevels have to be taken into account, because excitation with light combined with the spontaneous emission from the upper transition level induces a population transfer between them. These approximations prove to be adequate for not very high intensities, which are typical for holographic writing (see also the discussion in Section 6).

We take the master equation for atomic density matrix ρ in the presence of spontaneous emission in the form [13,14]:

$$\frac{\partial\rho}{\partial t}=(i/\hbar)[\rho,H]+\sum_{q=-1,0,1}C_q\rho C_q^{\dagger}-\frac{1}{2}(C_q^{\dagger}C_q\rho+\rho C_q^{\dagger}C_q). \tag{1}$$

Here H is the Hamiltonian of the isolated atom, and $C_q, C_q^{\dagger}$ are lowering and raising operators for the multilevel atom. The z axis for quantization is chosen along the wave propagation direction and parallel to the magnetic field. All operators ρ, H, C_q, and $C_q^{\dagger}$, are $N\times N$ matrices, with N a total sublevel number. The Hamiltonian is taken in dipole approximation; it has diagonal elements equal to state energies, and off-diagonal elements are proportional to the left- and right-circularly polarized components of the electric field of the wave. These elements couple states with $F_e-F_g=0,\pm1$, and $m_{Fe}-m_{Fg}=\pm1$, and they are proportional to dipole moments for a given transition.

The terms under the sum in the right-hand side describe spontaneous emission. Operators $C_q^{\dagger}, C_q$, are proportional to the atomic dipole operator:

$$C_q^{\dagger}|F_g,m_{Fg}\rangle=\Gamma^{1/2}(1,F_g,q,m_{Fg};F_e,m_{Fe}=m_{Fg}+q)F_e,m_{Fe}$$
$$=m_{Fg}+q>, \tag{2}$$

$$C_q^{\dagger}|F_e,m_{Fe}\rangle=0, \tag{3}$$

$$C_q=(C_q^{\dagger})^{+}, \tag{4}$$

with lifetime Γ and Clebsch–Gordan coefficients for coupling ground and excited states sublevels.

The standard rotating wave approximation is used to eliminate time-dependent expressions in the Hamil-

tonian. The dipole moments for transitions are calculated according to the expressions of [11].

Equation (1) is solved numerically. It has the form

$$\frac{\partial \rho}{\partial t} = \Lambda(\rho), \tag{5}$$

where $\Lambda(\rho)$ is a linear, time-independent operator acting on elements of the matrix ρ (it is represented by the $N^2 \times N^2$ matrix, which is applied to N^2 dimensional vector ρ, and cannot be reduced to a multiplication of ρ as $N \times N$ matrix by another $N \times N$ matrix). The formal solution is given by

$$\rho(t + \Delta t) = \exp(\Lambda \Delta t)[\rho(t)], \tag{6}$$

with an operator exponent. The numerical solution proceeds as a calculation of the operator exponent with the Taylor series and consequent application of it to $\rho(0)$, $\rho(\Delta t)$, etc. Since Λ is time-independent, the operator exponent for a given set of parameters is calculated only once. This method of solution works well up to $N \approx 18-20$, but the calculation time grows rapidly with N, because matrix exponent calculation time scales as N^6, and the rest of the algorithm implementation scales as N^4. We also have implemented another solution algorithm that is more efficient for big N. It was not used here, and we will discuss it elsewhere.

The initial condition is of equal population distribution among N_g ground sublevels $\rho_{ii} = 1/N_g$, for $1 \leqslant i \leqslant N_g$ and all other density matrix elements are zero. The time-dependent complex polarization of a medium for right/left circular polarization is obtained with a trace of dipole operator $P(t) = Tr(C_q \rho)$, $q = \pm 1$. The real and imaginary parts of polarization after dividing by field amplitude give absorption coefficient and phase shift per unit length for right- and left-polarized circular components. The result is averaged over time, necessary according to the Maxwell distribution for the atom to arrive to the center of circular beam with radius l_0:

$$P_a = \int_0^\infty P(t) \frac{\tau^2}{t^3} \exp(-\tau^2/t^2) \mathrm{d}t, \tag{7}$$

and characteristic time

$$\tau = l_0 \sqrt{\frac{M}{2k_B T}}, \tag{8}$$

with M as the atomic mass and $k_B T$ as the Boltzmann constant and temperature product.

One more averaging over different Doppler-shifted groups of atoms is performed to obtain absorption and refraction values measured in the experiment. We are interested in values close to the center of the absorption line; thus, to the first approximation, we assume here that all velocity groups of atoms have equal concentrations. By doing this, we do not consider effects, which are produced at the line edges, though such effects can be important for higher temperatures.

3. COMPUTER MODEL, RESULTS

From a macroscopic point of view, the changes in light intensity and polarization state affect the medium absorption coefficient and refractive index. If the vapor is illuminated with two coherent beams, the medium parameters vary in space according to local changes in polarization and/or intensity. This produces a holographic grating, which can be detected by diffraction of beams.

The information on local illumination is recorded in the atomic medium either in the form of sublevel populations, which are given by diagonal elements of the density matrix, or in the form of quantum coherences, given by the matrix off-diagonal elements. Long-living coherences between lower levels can be induced by the light of a single frequency if both circular polarizations are present, in particular, for linear polarization.

First, we discuss the case of strictly circular polarization of incident beams for which coherences between lower levels are absent. In this case, for the center of the line the grating is of the absorption type. Thus, to estimate diffraction it is sufficient to calculate an absorption as a function of light intensity. These dependences (Fig. 2) are qualitatively different for the $F_g = 2$ and $F_g = 1$ transition lines. For the transition with $F_g = 2$, the absorption for big intensities I behaves approximately as $(1 + I/I_S)^{-1/2}$, (I_S is saturation intensity close to $1-3$ mW/cm^2), and it is relatively independent on the probing beam diameter (time of transit). Such behavior follows from a simple, two-level model [15]. It is explained by noting that the transition from $F_e = 3$ to $F_g = 1$ is forbidden in dipole approximation, thus the atom with the excited $F_g = 2$ to $F_e = 3$ transition after some illumination time arrives to the isolated state with $m_{Fg} = \pm 2$, $m_{Fe} = \pm 3$ for right or left circular polarization, and the atom behaves essentially as having only two levels.

For the transition with $F_g = 1$, making the beam diameter bigger noticeably reduces the absorption, and the characteristic saturation intensity is much smaller than for the $F_g = 2$ transition. The absorption diminishes with

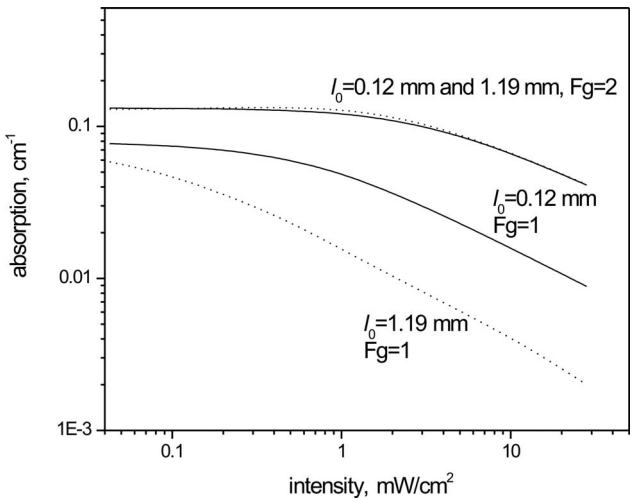

Fig. 2. Absorption calculation for circularly polarized light as function of intensity for $F_g = 1$ and $F_g = 2$ lines in the center of circular beam with uniform intensity distribution and radius $l_0 = 0.12$ mm (solid) and $l_0 = 1.19$ mm (dots). The calculation is made for natural Rb at temperature 30°C using data of [11].

intensity faster than $I^{-1/2}$. This occurs because the light-induced transitions from $F_g=1$ to $F_e=2$ transfer the population to the "unseen" level $F_g=2$ as a result of spontaneous emission. The lambda-transition $F_g=1$ to $F_e=0$, when isolated from level $F_g=2$, accumulates atoms under circular polarization in a state that is nonabsorbing. For transition $F_g=1$ to $F_e=1$, the combination of the above-mentioned factors works—the population is partly transfered to the $m_F=\pm 1$ state and partly to $F_g=2$ states. Thus, the absorption seen for the $F_g=1$ line is a result of a transient process and critically depends on the atoms that enter the beam from outside (the collisions inside a beam can be neglected because of low concentration of atoms). The time of the $F_g=1$ depopulation for small intensity becomes bigger than the transit time, and thus the absorption for small intensity tends to be a constant value, which does not depend on beam diameter.

The different characters of saturation produce marked differences in diffraction efficiency for absorption gratings in the $F_g=2$ and $F_g=1$ lines. In the $F_g=2$ case, the measured dependence of transmission on light intensity gives a good estimation for diffraction efficiency. At the $F_g=1$ transition, the width of the beam becomes important: close to the interference pattern center the atoms become "transparent;" they do not respond to local changes in illumination, and the diffraction efficiency is quite poor there.

The transition from $F_g=1$ becomes much more efficient for holography if quantum coherence effects, which arise for noncircular polarizations, are included, and a weak magnetic field is applied.

With a linearly polarized light, which is a superposition of right and left circular polarizations, the dark state is formed [16]. For zero detuning of both fields, the population of the upper level becomes zero, and wavefunctions for lower levels have fixed phase differences. The coherent state is destroyed with small frequency detunings in-

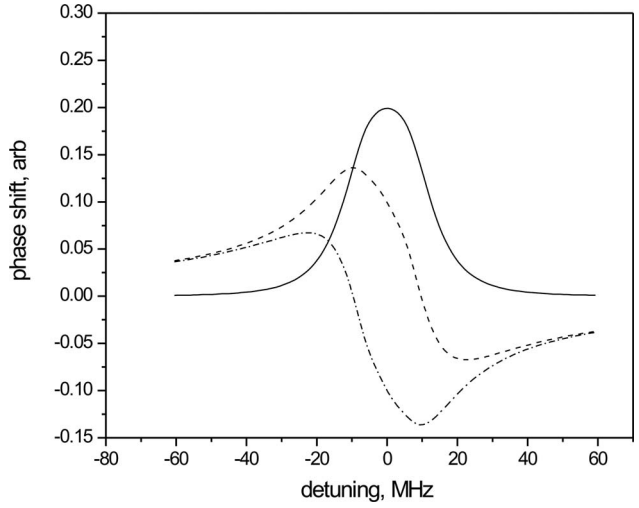

Fig. 3. Faraday rotation for $F_g=1$, $F_e=0$ transition. The numeric example shows that for nonzero magnetic field, refractive indexes for left (dash) and right circular polarizations (dash-dot) have different dependences on detuning from transition frequency. The difference (solid line) does not disappear if integrated with respect to detunings; thus, this mechanism is important for Doppler broadened line. Light intensity 2.13 mW/cm^2, magnetic field 0.12 G, beam radius $l_0=1.19$ mm.

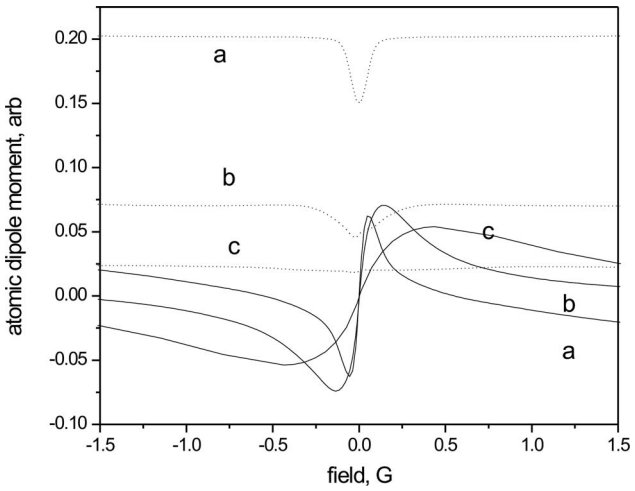

Fig. 4. Real and imaginary parts of calculated dipole moment divided by field amplitude, which are proportional to optical activity (solid) and absorption (dots) vs. magnetic field for different light intensities in $F_g=1$ line. Intensities are: a, 0.216 mW/cm^2; b, 2.13 mW/cm^2; c, 19.2 mW/cm^2; the beam radius is $l_0=1.19$ mm.

duced by the magnetic field. Because of this, sharp spectral features appear. The magnetic field splits Zeeman sublevels; this produces differences in propagation speeds for right- and left-polarized components, and the polarization plane rotates (nonlinear Faraday rotation [17]). The rotation mechanism is illustrated in Fig. 3 for the $F_g=1$, $F_e=0$ transition. The calculated rotation angle as a function of the magnetic field for different light intensities is presented in Fig. 4. The behavior is dominated here by two lambda systems formed in the $F_e=0$ and $F_e=1$ transitions. For big intensities, the simultaneous interaction of light with both $F_e=0$ and $F_e=1$ levels produces a diminishing of the rotation signal in comparison with independent level approximation. The difference between two calculation methods is around 1% for 0.2 mW/cm^2 intensity, $\approx$10% for 2 mW/cm^2 intensity, and grows to a significant 30% for 20 mW/cm^2. The independent level model does not give the experimentally observed drop in maximal possible rotation angle for higher intensities; it shows the maximal rotation angle is approximately the same for 20 and 2 mW/cm^2 instead.

For the $F_g=2$ line, the most important transition is to $F_e=3$, which is isolated from $F_g=1$. The character of rotation for the $F_g=2$ line is different than for $F_g=1$. The maximal rotation angle grows with intensity here in all the investigated intensity intervals (Fig. 5).

The polarization rotation is basically the change in the refractive index. Because of the nature of a coherent state, the absorption of an atom in this state is reduced (light-induced transparency). For a zero magnetic field the rotation is zero, but for small magnetic fields and polarizations close to a linear magnetic field, enhanced Kerr nonlinearity can be expected [18]. The growth in the intensity makes the rotation-to-absorption ratio bigger, which produces a more pronounced phase hologram.

It is also interesting to look at the absorption for linear polarization as a function of magnetic field B. Here, the characteristic behavior is also different for $F_g=1$ and $F_g=2$ transitions. For $F_g=1$, coherence effects produce a nar-

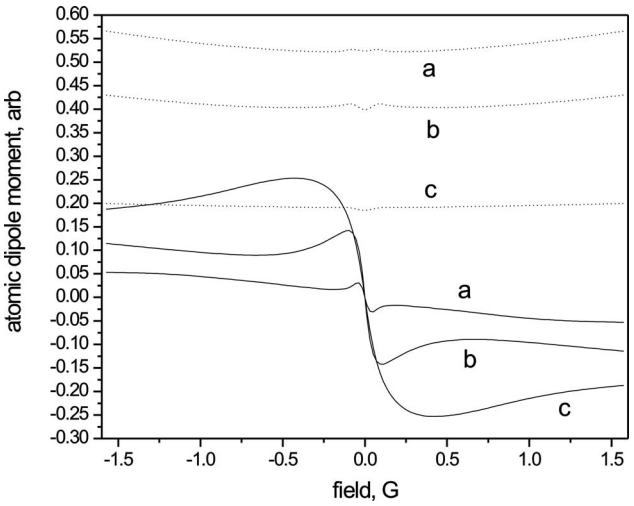

Fig. 5. The same as in Fig. 4, but for $F_g=2$ line.

row spike in transmission at a magnetic field close to zero. At $F_g=2$, the spike is much wider, and it has fine structure for a small B.

4. EXPERIMENT, ABSORPTION AND ROTATION MEASUREMENTS

In the experiment we used a 50 mm long, 2.5 cm diameter rubidium cell. It was placed inside a solenoid and protected from the geomagnetic field with two concentric cylindrical shells made from an alloy with high magnetic permeability. The estimation of the residual field based on small-field features in absorption curves, such as those depicted in Fig. 4, curve "a," gives values ≈ 0.02 G for the residual longitudinal component. (To make this estimation we were measuring the solenoid current at transmission maximum.) The electric heater used to control the temperature was made with a twisted pair of wire and placed outside of the first protective layer to reduce the influence of the magnetic field of the heater. The cell was locally cooled with a weak air flow to prevent rubidium deposition on the windows. The elliptical laser beam of a tunable semiconductor laser (<50 mW, 780.24 nm wavelength) was expanded with a telescopic lens system to approximately a 3×5 mm size. The quarter-wave plate and polarizers served for polarization control.

In the first series of experiments we measured the absorption for circularly polarized light as a function of intensity at a nominally zero magnetic field. The circular diaphragm was placed in front of the cell in the central part of the Gaussian beam. The intensity distribution across the diaphragm was close to uniform, with variations typically smaller than 10%. The light intensity after the cell was measured at the center of a beam by a photodetector with a 0.5 mm diameter aperture. The temperature of 30 °C was chosen to ensure that the absorption was not very high, and the intensity did not vary much along the cell.

The results are presented in Fig. 6. It is seen that the computer model gives quite an accurate description of absorption dependence on intensity for both $F_g=1$ and $F_g=2$ transitions. Note that the only fitting parameter used

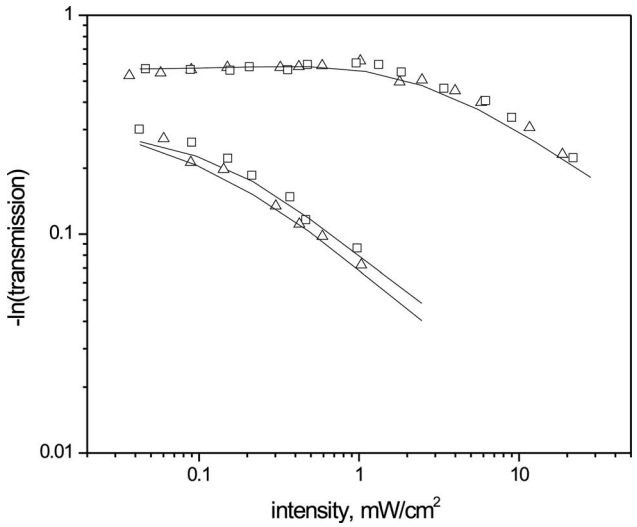

Fig. 6. Transmission logarithm for 50 mm long cell at 30 °C for circularly polarized beam with radius $l_0=1.19$ mm (triangles) and $l_0=0.78$ mm (squares). Upper curve—$F_g=2$ line, lower—$F_g=1$. Solid lines are theory for corresponding beam radius (also see Fig. 2). For $F_g=2$ transition, the theory gives very close curves, and only $l_0=1.19$ mm one is shown. To fit the data we used the vapor density, which is approximately 10% lower than the value found according to [11].

here is the vapor density, common for both lines—the intensity scale is absolute, and the true beam diameter was used in the calculation. The fitting vapor density value is about 10% smaller than the one taken from [11] and used in Fig. 2 ($1.5\cdot10^{10}$ cm^{-3}). For $F_g=1$, the difference in absorption between apertures with 0.78 mm and 1.19 mm radii is clearly seen and generally corresponds to the theory as well as absolute absorption values. We did not perform experiments with much smaller apertures, because diffraction effects are pronounced in this case.

The nonlinear Faraday rotation was measured using a 45° rotated polarizer with a technique described in [5]. Note that the raw data $v(B)=[I_p(B)-I_p(0)]/I_p(0)$ (where $I_p(B)$ is the detector signal as function of magnetic field)

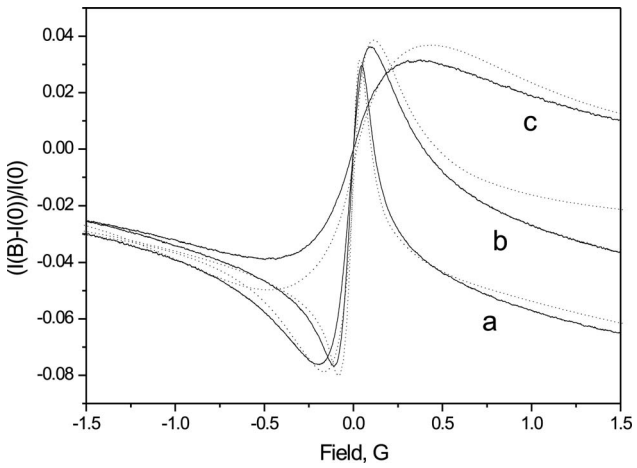

Fig. 7. Photodetector signal after 45° turned polarizer as function of magnetic field for linear input polarization and different light intensities in $F_g=1$ line (solid). Intensity values and beam radius are the same, as those used for calculation in Fig. 4. Temperature 30°C. Dashed lines are theoretical curves.

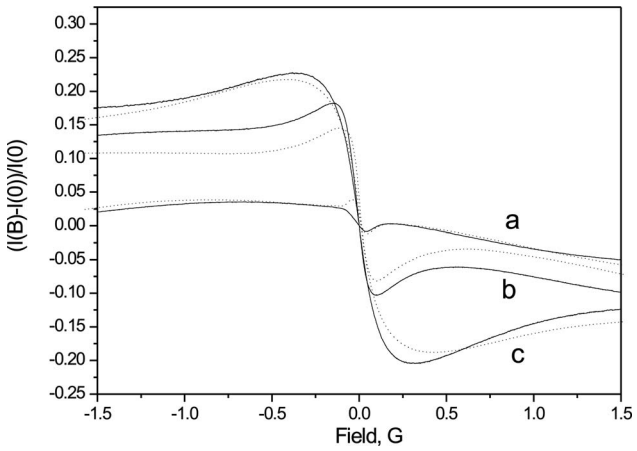

Fig. 8. The same as in Fig. 7, but for $F_g=2$ line.

cannot be used as the direct measure of Faraday rotation because of noticeable influence of the magnetic-field-induced absorption (Figs. 4 and 5). In particular, the obtained curve is not antisymmetric with respect to the magnetic field $[\upsilon(-B)\neq-\upsilon(B)]$, as it must be for pure Faraday rotation. It is easy to see that the resulting curve in the approximation of a small signal is the sum of a term proportional to the absorption curve discussed earlier and a term proportional to the Faraday rotation angle. For a 45° rotated polarizer, the two curves enter with equal coefficients. Thus, we have compared the experimental curves in Figs. 7 and 8 with the combination of theoretically calculated absorption and rotation. The theoretical curves are shown with dots; all are taken for the same vapor density.

It is seen that the theory gives a generally adequate description of complicated polarization behavior, including good predictions for relative rotation magnitudes in two different lines. The signs of rotation for small magnetic fields in two lines are opposite, as predicted by the theory.

We measured light absorption dependence on the magnetic field for linearly polarized light as well. These curves also correspond quite well to the theory. The narrow spike, obtained in the $F_g=1$ line for small intensity, is a good indicator of a zero magnetic field condition. For the $F_g=2$ line, the magnetic-field-induced transmission spike is much wider than for $F_g=1$, and it has an additional narrow feature around the zero magnetic field. The small field feature in the $F_g=2$ line changes its form when the frequency is scanned inside the line; thus, some minor effects exist there, which are not taken into account by our theoretical analysis. The general character of the spike is reasonably well reproduced by theory, though the agreement is somewhat worse here than for $F_g=1$.

5. EXPERIMENT, HOLOGRAM WRITING

In our experiment the Bragg regime is realized if the angle between writing beams is bigger than approximately 5 mrad. In two-wave mixing experiments a dynamic hologram is often detected by closing the signal beam and monitoring the diffraction of a reference wave in the direction of the signal. For rubidium, the writing/erasing time can be less than 100 ns; this makes such a method quite complicated technically.

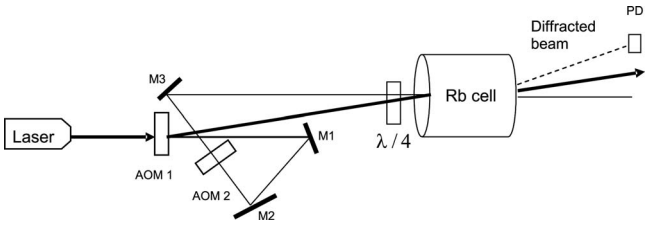

Fig. 9. Experimental setup. AOM 1,2 are acousto-optical modulators; M1-M3 are mirrors; PD is photodetector. The angle between writing beams is exaggerated for better visibility. The second modulator produces the frequency-shifted beam slightly above the picture plane.

Because of this, for measurements we crossed a strong reference beam and a weak signal beam at a sufficiently small angle to obtain a non-Bragg (conjugated) diffraction order, produced by the diffraction of a strong beam on the grating written by it with a signal. The basic configuration here is three-wave mixing. A small angle also helps to keep the interacting beams with a good overlap. A similar setup was used in [5].

The experiment is depicted in Fig. 9. Two acousto-optical modulators (AOM), one fixed at an 80 MHz frequency and another tuned between 65 MHz and 95 MHz, were used to shift the frequency of a signal wave in a ±15 MHz interval with respect to the reference. A reference beam and a weaker signal were crossing inside the cell at an angle of 2.6±0.3 mrad. The intensity ratio of 10:1 was kept frequency-independent by adjusting the high-frequency signal to a signal beam modulator. Applying amplitude modulation to the AOM, we could switch the signal beam on and off with a characteristic time of 100–200 ns, determined by the beam width.

For efficient holgram writing the temperature has to be high enough, and this produces strong absorption. Raising the temperature even more results in the diminishing of the diffraction signal, because absorption dominates the output intensity. There is the optimal writing temperature, which depends on beam parameters, and it is different for $F_g=1$ and $F_g=2$ transitions. The simplest method for hologram writing in Rb is to use circular polarization and amplitude grating at the $F_g=2$ line. This can be done at the zero magnetic field, and the magnetic field influence is not significant. If the total absorption is not very big because of high temperature, the signal is maximal close to the center of the line. The diffraction efficiency reasonably corresponds to the estimation made with the known dependence of absorption on light intensity. The maximal efficiency obtained for $T=91°\mathrm{C}$ is ≈1%, consistent with characteristic values for amplitude holograms. Note that gratings with efficiencies somewhat higher than those shown in figures can be written with equal beam intensities.

In Figs. 10 and 11 we show diffraction efficiency dependences on frequency detuning for two light intensities. For circular polarization and small intensity (Fig. 10), the cutoff frequency $\nu=8.5\pm0.5$ MHz (as taken by a two-times drop in diffraction efficiency) gives characteristic writing time $\tau_R=(2\ \pi\nu)^{-1}\approx20$ ns. This time is comparable with the upper level lifetime (25 ns), and becomes somewhat

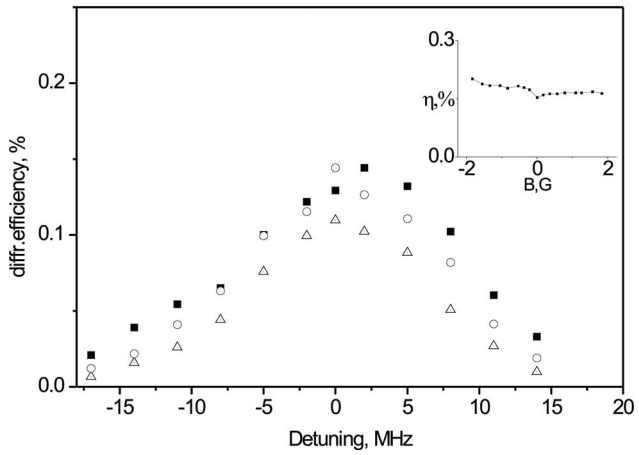

Fig. 10. Diffraction efficiency at the center of $F_g=2$ line for average light intensity $I=7.5$ mW/cm^2 vs. detuning between writing beams; squares are circular polarization and zero magnetic fields; triangles are plane polarization and zero magnetic fields; circles are plane polarization and magnetic fields $B=0.65$ G. Insert shows dependence of diffraction intensity on magnetic field for plane polarization $T=91°C$.

smaller for bigger intensity. When the signal beam is switched on and off, as described earlier, no transient processes are seen in diffraction at times >100 ns, which we can resolve directly.

The diffraction efficiency η for the $F_g=2$ transition can be improved by using linear polarization and a weak magnetic field. The dependences of η on the magnetic field at zero detuning are shown in the insets. It is seen that for small intensity, the magnetic field application does not produce a big change, but for higher intensities the influence is well-pronounced. At the magnetic field, which gives the maximal signal, the spike around zero detuning appears, and its width gives a characteristic time comparable to the flight of time across the fringe (Fig. 11). The transient processes are seen at the submicrosecond scale after opening/closing the signal beam, and the transient processes can have a shape of exponential relaxation with more than one characteristic time, or strongly damped oscillation, depending on the magnetic field. The relaxation time corresponds to characteristic frequency detunings in the central spike.

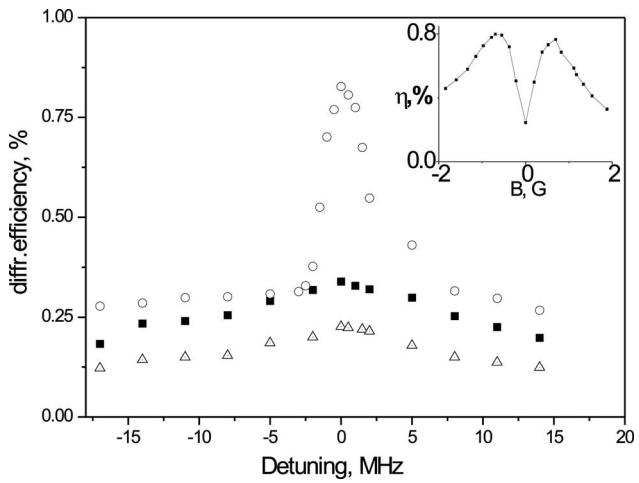

Fig. 11. The same as in Fig. 12, but for light intensity $I=67$ mW/cm^2. Dependence of diffraction efficiency on detuning for plane polarization is taken for $B=0.6$ G, which gives the maximum in field dependence (inset).

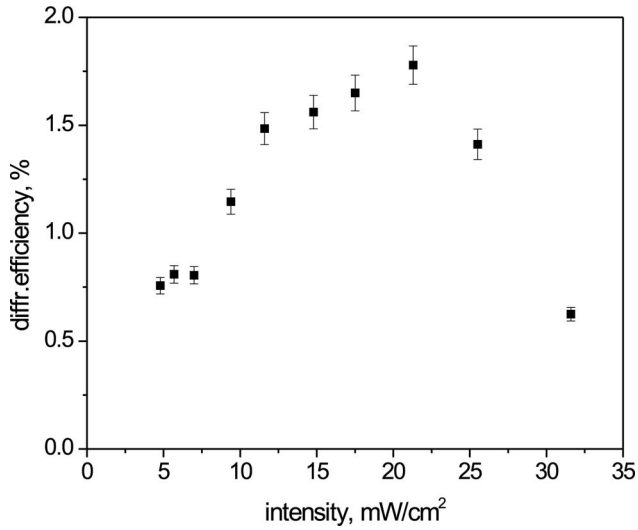

Fig. 12. Dependence of diffraction efficiency for plane polarization on light intensity for $F_g=1$ transition at zero frequency detuning between beams. The magnetic field for each measurement was taken to produce maximal diffraction; the temperature is $T=113°$C.

For the $F_g=1$ transition the circular polarization writing is not efficient. For plane polarization, different from the situation with $F_g=2$, the maximum in diffraction efficiency is obtained for intensities 10–25 mW/cm^2 and diminishes if the intensity is bigger (Fig. 12). This is related to the drop in rotation for big intensities, discussed in the previous section and in the theoretical section. Efficient writing is obtained for the nonzero field (Fig. 13, inset), and the signal as a function of detuning between writing beams strongly diminishes for 1–2 MHz detunings. Making intensity smaller does not change the character of this curve. The transient processes are seen after opening and closing the beam, similar to those observed for $F_g=2$. The

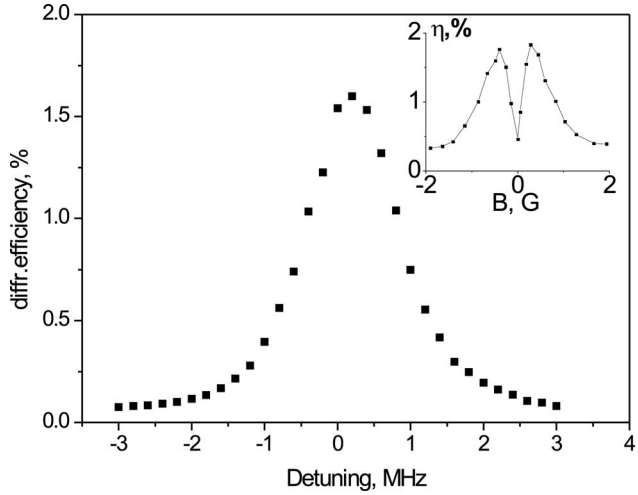

Fig. 13. Dependence of diffraction efficiency for plane polarization on frequency detuning between writing beams for $F_g=1$ transition for magnetic field 0.28 G and its dependence on magnetic field for zero detuning (inset). Light intensity is $I=22$ mW/cm^2; the temperature is $T=113°$C.

temperature, for which the diffraction is efficient, is higher here than for $F_g=2$ because both absorption and optical rotation per atom are smaller, and higher vapor densities are needed.

For mechanisms with polarization rotation we observe trade-off between diffraction efficiency and writing time, which is usual for dynamic holography.

6. DISCUSSION AND CONCLUSIONS

The experiments we performed were intended mostly to establish the general validity of the proposed theory; thus, the systematic errors could in some cases be as big as 10%. In particular, we did not use antireflecting coating for the rubidium cell, the nonuniformity in illumination across the aperture was around 10%, and we did not measure small absorptions in the $F_g=1$ transition with good precision. To avoid vapor density recalculations, we performed all rotation and absorption measurements for the same temperature of 30 °C, and we could not satisfy the condition of small absorption in all intensity ranges. The theory does not take into account systematically simultaneous interaction of light with adjacent F levels and a finite Doppler line width. For bigger intensities these two factors become more important. In particular, the influence of resonant self-rotation of elliptically polarized light cannot be neglected (we do not treat elliptical polarizations here).

However, for moderate intensities practically interesting for holography, the theory adequately describes the behavior of observed absorption and optical rotation, and it can be used as a guide for experimental investigation as well as for comparison with simplified theoretical approximations.

For holographic writing in ^{87}Rb close to resonance it is possible to employ absorption gratings for the $F_g=2$ line. Though the diffraction efficiency in this case is limited by $\approx 1\%$, the sensitivity is high, writing time can be as small as 20 ns, and there is no need for strict polarization and magnetic field control. The absorption grating for the $F_g=1$ transition is inefficient for the reasons explained in the theoretical section.

To obtain a more efficient grating with phase component at resonance wavelength, it is necessary to overcome absorption, thus the light intensity grows. Here, the magnetic field and polarization control are essential. The $F_g=1$ transition is easily saturated, but much of the saturation comes from the "useless" population transfer to the $F_g=2$ level. With higher temperatures, the gratings with bigger diffraction efficiency than those for the amplitude grating in $F_g=2$ can be written. Generally, more efficient gratings require bigger writing time, and this can become a problem for smaller fringe spacings when the time of flight across a fringe diminishes.

Holographic cw writing with two beams of nearly equal frequencies is experimentally the simplest, but it seems probable that more favorable conditions can be obtained with additional illumination at another frequency and/or by using nonstationary mechanisms. The rich level structure of rubidium provides many possibilities for manipulation.

In conclusion, we demonstrate that the density matrix formalism with a big number of sublevels taken into account gives a generally adequate description of processes important for holographic grating formation in rubidium vapor at moderate intensities. The analysis clarifies the different factors involved, in particular the role of time of transit (beam diameter and fringe spacing). Some situations such as the absorption grating at $F_g=2$ permit simple analytical approximations, but it seems that no simple model can account for complicated polarization behavior, which gives efficient phase gratings for strongly saturated lines.

REFERENCES

1. P. Günter and J.-P. Huignard, eds., *Photorefractive Materials and Their Applications 3*, Vol. 115 of Springer Series in Optical Sciences (Springer Verlag, 2007).
2. M. P. Petrov, S. I. Stepanov, and A. V. Khomenko, *Photorefractive Crystals in Coherent Optical Systems*, Vol. 59 of Springer Series in Optical Sciences (Springer Verlag, 1991).
3. T. T. Grove, E. Rousseau, X.-W. Xia, D. S. Hsiung, M. S. Shahriar, and P. R. Hemmer, "Efficient and fast optical phase conjugation by use of two-photon-induced gratings in the orientation of angular momentum," Opt. Lett. **22**, 1677–1679 (1997).
4. X.-W. Xia, D. Hsiung, P. S. Bhatia, M. S. Shahriar, T. T. Grove, and P. R. Hemmer, "Polarization selective motional holeburning for high efficiency, degenerate optical phase conjugation in rubidium," Opt. Commun. **191**, 347–351 (2001).
5. N. Korneev and J. Soto, "The nonlinear Faraday rotation-based dynamic holography in rubidium vapor," Opt. Commun. **245**, 437–442 (2005).
6. V. Tikhonenko, J. Christou, B. Luther-Davis, and Y. S. Kivshar, "Observation of vortex solitons created by the instability of dark soliton stripes," Opt. Lett. **21**, 1229–1231 (1996).
7. V. Tikhonenko, Y. S. Kivshar, V. V. Steblina, and A. A. Zozulya, "Vortex solitons in a saturable optical medium," J. Opt. Soc. Am. B **15**, 79–86 (1998).
8. J. A. Andersen, M. E. J. Friese, A. G. Truscott, Z. Ficek, P. D. Drummond, N. R. Heckenberg, and H. Rubinsztein-Dunlop, "Light guiding light: nonlinear refraction in rubidium vapor," Phys. Rev. A **63**, 023820 (2001).
9. C. F. McCormick, D. R. Solli, R. Y. Chiao, and J. M. Hickman, "Saturable nonlinear refraction in hot atomic vapor," Phys. Rev. A **69**, 023804 (2004).
10. C. F. McCormick, D. R. Solli, R. Y. Chiao, and J. M. Hickman, "Nonlinear absorption and refraction in near-detuned rubidium vapor," J. Opt. Soc. Am. B **20**, 2480–2483 (2003).
11. D. A. Steck, "Rubidium 87 D line data," online reference http://steck.us/alkalidata.
12. A. N. Nesmeyanov, *Vapor Pressure of the Chemical Elements* (Elsevier, 1963).
13. G. S. Agrawal, *Quantum Statistical Theories of Spontaneous Emission and Their Relation to Other Approaches* (Springer Verlag, 1974).
14. K. Mølmer, Y. Castin, and J. Dalibard, "Monte Carlo wave-function method in quantum optics," J. Opt. Soc. Am. B **10**, 524–538 (1993).
15. V. S. Letokhov and V. P. Chebotayev, *Nonlinear Laser Spectroscopy* Vol. 4 (Springer Verlag, 1977).
16. E. Arimondo, "Coherent population trapping in laser spectroscopy," in *Progress in Optics*, E. Wolf, ed. (Elsevier Science, 1996), Vol. 35, pp. 257–354.
17. D. Budker, W. Gawlik, D. F. Kimball, S. M. Rochester, W. Yashchuk, and A. Weis, "Resonant nonlinear magneto-optical effects in atoms," Rev. Mod. Phys. **74**, 1153–1201 (2002).
18. A. B. Matsko, I. Novikova, G. R. Welch, and M. S. Zubairy, "Enhancement of Kerr nonlinearity by multiphoton coherence," Opt. Lett. **28**, 96–98 (2003).